

RESEARCH

Open Access



Improving accelerated 3D imaging in MRI-guided radiotherapy for prostate cancer using a deep learning method

Ji Zhu^{1†}, Xinyuan Chen^{1†}, Yuxiang Liu^{1,2}, Bining Yang¹, Ran Wei¹, Shirui Qin¹, Zhuanbo Yang¹, Zhihui Hu¹, Jianrong Dai¹ and Kuo Men^{1*}

Abstract

Purpose This study was to improve image quality for high-speed MR imaging using a deep learning method for online adaptive radiotherapy in prostate cancer. We then evaluated its benefits on image registration.

Methods Sixty pairs of 1.5 T MR images acquired with an MR-linac were enrolled. The data included low-speed, high-quality (LSHQ), and high-speed low-quality (HSLQ) MR images. We proposed a CycleGAN, which is based on the data augmentation technique, to learn the mapping between the HSLQ and LSHQ images and then generate synthetic LSHQ (synLSHQ) images from the HSLQ images. Five-fold cross-validation was employed to test the CycleGAN model. The normalized mean absolute error (nMAE), peak signal-to-noise ratio (PSNR), structural similarity index measurement (SSIM), and edge keeping index (EKI) were calculated to determine image quality. The Jacobian determinant value (JDV), Dice similarity coefficient (DSC), and mean distance to agreement (MDA) were used to analyze deformable registration.

Results Compared with the LSHQ, the proposed synLSHQ achieved comparable image quality and reduced imaging time by ~66%. Compared with the HSLQ, the synLSHQ had better image quality with improvement of 57%, 3.4%, 26.9%, and 3.6% for nMAE, SSIM, PSNR, and EKI, respectively. Furthermore, the synLSHQ enhanced registration accuracy with a superior mean JDV (6%) and preferable DSC and MDA values compared with HSLQ.

Conclusion The proposed method can generate high-quality images from high-speed scanning sequences. As a result, it shows potential to shorten the scan time while ensuring the accuracy of radiotherapy.

Keywords Accelerated 3D MRI scanning, High-quality MRI image, Cycle-consistent adversarial networks, Image quality, Deep learning, 1.5 T MR-linac

[†]Ji Zhu and Xinyuan Chen are co-first authors and contributed equally to this work.

*Correspondence:

Kuo Men

menkuo126@126.com

Full list of author information is available at the end of the article



Introduction

MR-linac is an innovative linear accelerator integrated with a magnetic resonance imaging (MRI) system. It enables the use of online adaptive planning based on the daily patient anatomical changes during every fraction [1–4]. The imaging system of Unity (Elekta) can currently provide 1.5 T low-speed, high-quality (LSHQ 3D) and high-speed, low-quality (HSLQ 3D) sequences for daily adaptive planning and position-validation. The LSHQ sequence can provide high-quality daily MR images, but its scan time is long for adaptive radiotherapy. The scan time of the HSLQ sequence (about 117 s) is much shorter than that of LSHQ sequence (about 411 s); however, the inferior image quality does not provide sufficient anatomical detail for daily radiotherapy. High quality image can provide both the extent and position of a tumor precisely, so as to irradiate tumors with high accuracy. However, this time-consuming issue is a significant challenge for MRI-based adaptive radiotherapy. Long scan times mean that the patient is likely to become uncomfortable and move [5]. The case of spontaneous movements will generate motion artifacts around the organ of interest.

One way to reduce scan time is to employ a high-speed acquisition sequence to acquire under-sampled MRI and then improve its quality by postprocessing. Researchers have presented several conventional methods to restore under-sampled MRI images to achieve high-quality images. These methods, which include linear regression [6], compressed sensing [7, 8], and random forest [9, 10], can provide high quality MR images with short time. These conventional techniques can generate MR images with a high signal-to-noise ratio and a short scan time. However, the influence of extracting hand-crafted features and the difficulty of modulating parameters to optimize performance limit their utility for routine clinical applications [11].

An alternative method to obtain high-quality MR images from low-quality MR images is to apply a deep learning approach. Several researchers have used generative adversarial network (GAN) to produce high-quality MR images by inputting low-quality MR images [12, 13]. The task of improving the quality of under-sampled MR images using U-net was also reported [11, 14]. These studies provide several potential solutions to solve the problem of long MRI scan time for daily MR-linac applications [11–14]. However, applying deep learning in high-quality image generation is often challenged by limited training data, since it can be expensive and time-consuming to acquire enough paired-data of real-world patients in MR-linac.

In this paper, we proposed a deep learning method that could steadily improve image quality for accelerated 3D imaging. To address the difficulty of collecting

patient data on MR-linac, we proposed a data augmentation technique to generate pseudo-linac MRI from simulation MRI for model pre-training. To the best of our knowledge, this is the first attempt to restore the image quality for high-speed scanning for the MR-linac. Different from most of current research, we used the real MR images, not the simulated images, to train the deep learning model. The results indicated that our method could achieve higher quality image compared with high-speed MR scanning and save 66% of the total generation time compared with low-speed MR scanning. The proposed method also can improve the accuracy of image registration for radiotherapy.

Methods

Data acquisition

Daily-MRI data were collected from 19 patients with prostate cancer who received MRI based adaptive radiotherapy (ART) from May 2021 to July 2022. Daily MRI scanning was performed on Unity MR-linac (Elekta, Stockholm, Sweden) using T2 3D LSHQ and T2 3D HSLQ sequences within 30 min, respectively. Sixty pairs of 1.5 T MR images in total from nineteen patients who received ART were retrospectively analyzed in this study. The number of collected paired image sets (LSHQ and HSLQ images) varied from 2 to 5 pairs for each patient. Imaging data of LSHQ and HSLQ images were 20,400 slices, respectively, for model training. The acquisition time of HSLQ (T2 3D Tra 2 min) and LSHQ (T2 3D Tra) sequence were 117 s and 411 s respectively. The MRI imaging protocols of HSLQ and LSHQ were shown in Additional file 1: Appendix A.

Furthermore, Images of 139 patients with prostate cancer were collected to train a data augmentation model to increase the size and diversity of the training set. Twenty of them, who were not included in the training of main model (19 patients), had 3.0 T simulation MR, LSHQ MR, and HSLQ MR images (2D slices: $n=6800$). Simulation-MRI scanning was performed using a 3.0 T MRI simulator (Discovery MR750w, GE Healthcare) with a T2-fs-propeller sequence. The Simulation-MRI imaging protocols were shown in Additional file 1: Appendix A.

Institutional Review Board approval was obtained for this retrospective analysis, and the requirement to obtain informed consent was waived. All the patient data were de-identified.

Data augmentation and training

To train an effective model, deep learning-based data-augmentation was applied to increase the size and diversity of the training set. The workflow of data-augmentation and the training step were shown in Fig. 1. Two cycle-GAN models, which was trained by twenty

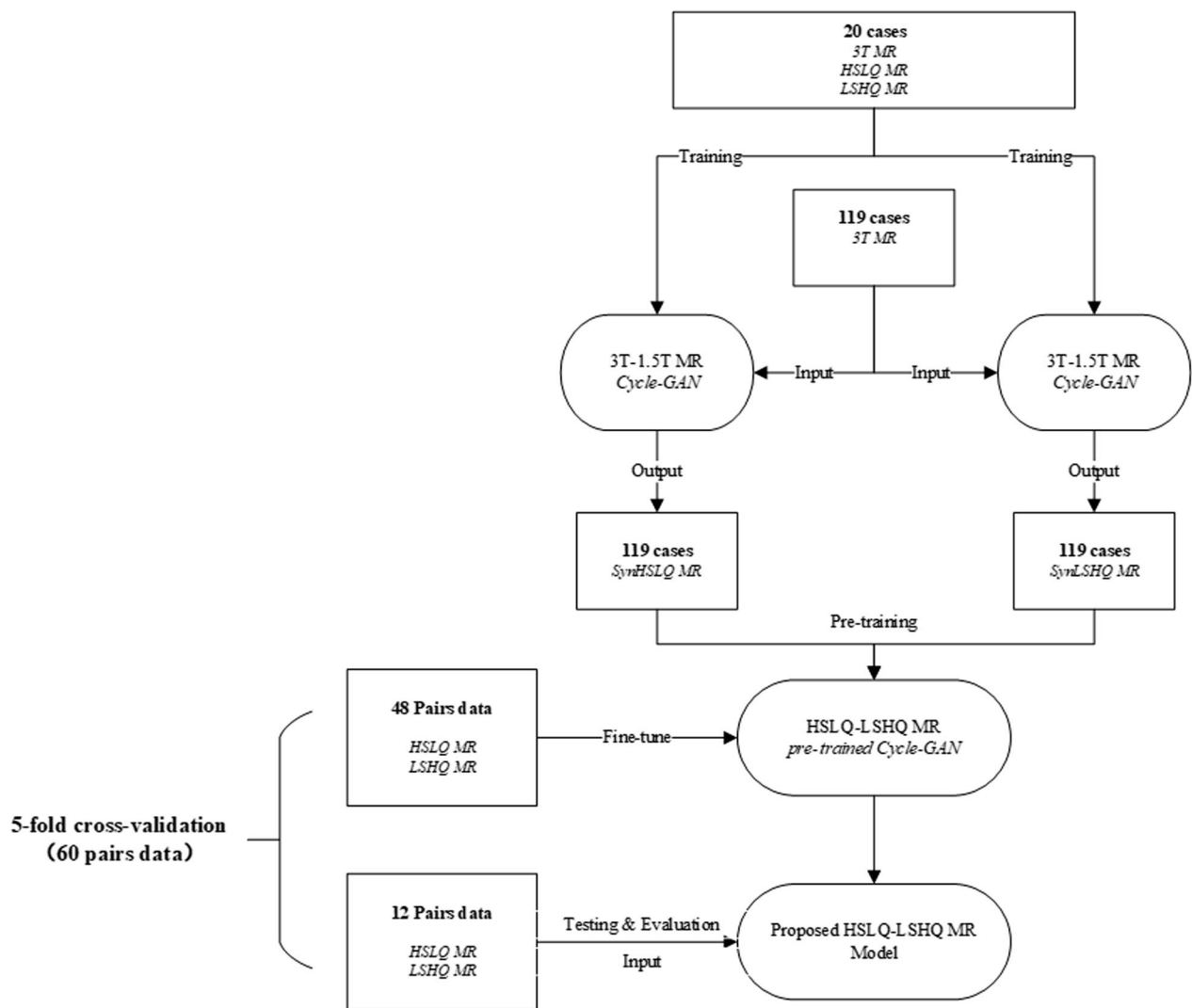


Fig. 1 The workflow of data-augmentation and the training

pairs of 3.0 T simulation MR, LSHQ MR, and HSLQ MR images, that can transform 3.0 T simulation MR images to synthetic HSLQ or synthetic LSHQ MR images were trained. Secondly, 3.0 T simulation MR images of the remaining 119 patients were enrolled into two cycleGAN models to generate 119 sets of synthetic HSLQ and LSHQ MR images. Subsequently, a pre-trained model for high-resolution MR image generation was trained with these paired synthetic MR images.

To restore the image quality of high-speed scanning for the MR-linac, we used 60 pairs (from 19 patients) of daily MR images, including LSHQ and HSLQ MR images, to fine-tune the pre-trained model.

Deep learning framework

Figure 2 shows the workflow of the training and testing stages in the proposed framework. We employed a CycleGAN which consisted of two discriminators (D) and two generators (G) to learn the mapping between the HSLQ and LSHQ images [15]. When testing the trained model, synthetic LSHQ images were predicted by the Generator AB of CycleGAN with HSLQ images as the input [16]. The CycleGAN model is expected to obtain high-quality synthetic LSHQ (synLSHQ) images from the HSLQ images with high acquisition speed. The details of the generator and discriminator are shown in Additional file 1: Appendix B.

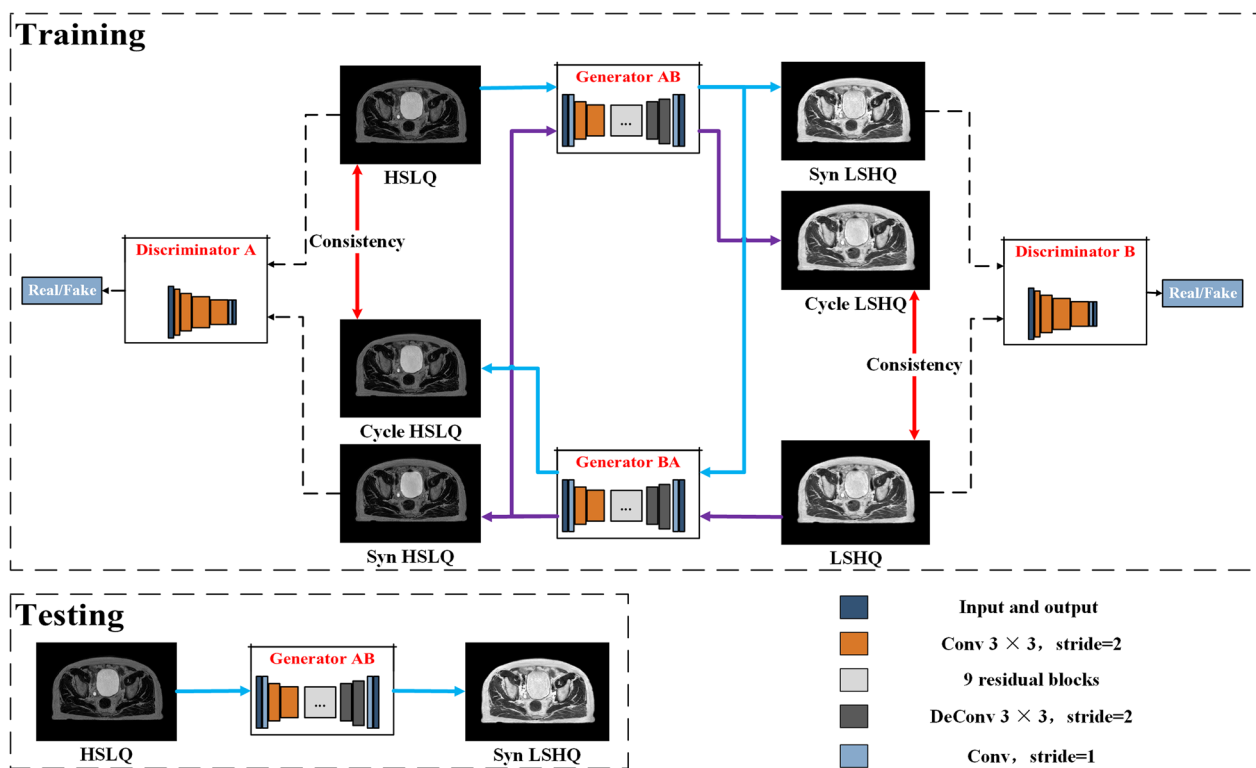


Fig. 2 Illustration of the training and testing part of the CycleGAN framework

Experiment

The five-fold cross-validation technique was employed to evaluate the proposed method. Here the data set (60 pairs of daily MR images) was split into 5 folds for the cross-validation [17]. Data for the same patient were selected into the same fold. During the first iteration, the first four folds (2D slices: 16,320) were used to fine-tune the model and the remaining one-fold (2D slices: 4080) was used to test the model. This process was repeated until each of the 5 folds was enrolled as the test set. In this experiment, model training and testing were done on an Nvidia GeForce RTX 3090 GPU.

Evaluation

The benefit of the proposed synLSHQ, which was generated by our model, was analyzed in image quality, and registration accuracy.

Efficiency

The acquisition time of HSLQ, LSHQ and synLSHQ generation time is recorded so as to evaluate the efficiency of our proposed method.

Image quality

HSLQ and the proposed synLSHQ images were rigidly registered to the reference ones before the evaluation of

image quality. The LSHQ images were set as the reference to evaluate the quality of HSLQ and the proposed synLSHQ images. The indices included the normalized mean absolute error (nMAE) [18, 19], structural similarity index measure (SSIM) [20], peak signal-to-noise ratio (PSNR) [21], and edge keeping index (EKI) [22]. Lower nMAE, larger SSIM, greater PSNR, and higher EKI values indicated better quality synthetic images. The definition of these evaluation indexes is presented in Additional file 1: Appendix C.

Registration accuracy

The daily LSHQ images were deformable registered against the planning CT to perform online adaptive radiotherapy process in clinic. Therefore, we evaluated the effect of image quality on deformable registration accuracy. The workflow of registration analysis is shown in Fig. 3. The synLSHQ and HSLQ images were deformably registered to the planning CT images, respectively. Jacobian determinant value (JDV) and geometric indices, which are two methods recommended by the AAPM Task Group 132 [23, 24], were used to analyze the registration accuracy. The average JDV close to 1 indicates a better registration [24]. The CTV and OARs were manually contoured on the planning CT, deformed HSLQ, and synLSHQ images by

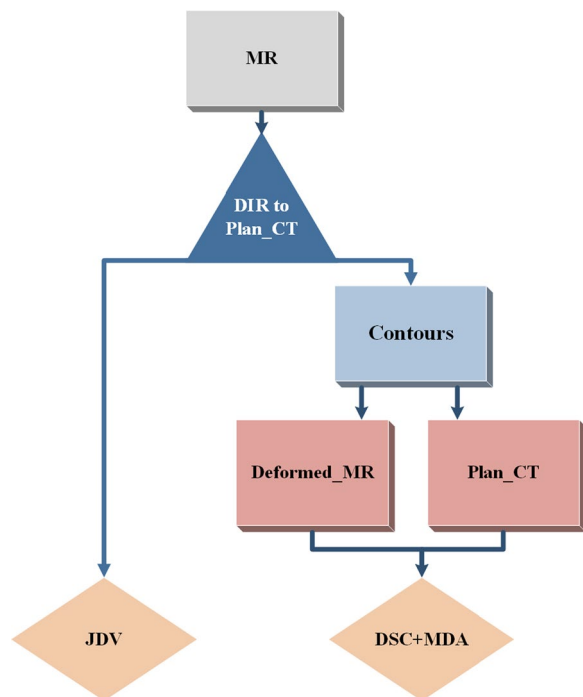


Fig. 3 Workflow of Registration analysis. Evaluation metrics of registration: Jacobian determinant value (JDV); Dice similarity coefficient (DSC); Mean distance to agreement (MDA)

an experienced clinician. The contours were reviewed by two senior clinicians. The consistency of the corresponding region of interest on planning CT and MR images can reflect registration accuracy. The geometric indices included the Dice similarity coefficient (DSC) and mean distance to agreement (MDA). A higher DSC and lower MDA indicate better image registration.

Results

Here, the performances of the synLSHQ images generated by the proposed method are analyzed by efficiency, image quality, and registration accuracy.

Efficiency

The total averaged generation time (s/case) of our proposed method included HSLQ acquisition time (approximately 117 s) and synLSHQ generation time (approximately 22.6 s). Compared with the existing LSHQ acquisition approach that generally requires 411 s/case, our highly efficient model (total generation time: 139.6 s) yields greater promise to generate synLSHQ images for routine clinical use. Our proposed method (including HSLQ and synLSHQ generation time) saved a total time of up to 66% compared with the LSHQ scanning approach.

Image quality

The results of image quality analysis between HSLQ and synLSHQ against the LSHQ images are shown in Table 1. The synLSHQ images generated by our method exhibited superior image quality with nMAE dropping by 57%, SSIM rising by 3.4%, PSNR increasing by 26.9%, EKI ascending by 3.6% compared with the HSLQ images, respectively. The statistical analysis in Table 1 further indicates that the image quality of the synLSHQ images was improved significantly compared with that of HSLQ ($p < 0.01$ for nMAE, SSIM, PSNR, and EKI).

Figure 4 shows examples and corresponding zoom-in views of HSLQ, LSHQ, and the generated synLSHQ images. The zoom-in areas include the bladder and boundary of the pubic symphysis and prostate. The first two rows in Fig. 4 show that the boundary and soft tissue around the pubic symphysis and prostate in the synLSHQ image were easier to distinguish compared with that in the HSLQ images. The sky-blue arrow in the synLSHQ images shows a clear boundary and lower noise around the pubic symphysis. The synLSHQ images also provide a favorable image quality around the prostate (red arrow) compared with the HSLQ images.

The third and fourth row in Fig. 4 show that the streak artifacts appearing around the boundary of bladder (Red box) in the HSLQ images were corrected in the synLSHQ images. The synLSHQ images were more consistent with the LSHQ images.

Table 1 Quantitative image quality analysis between synLSHQ and HSLQ versus LSHQ images

	nMAE Mean ± sd	SSIM Mean ± sd		PSNR (dBs) Mean ± sd	EKI Mean ± sd
HSLQ–LSHQ	0.14 ± 0.04	0.87 ± 0.02	HSLQ	20.95 ± 2.21	0.55 ± 0.06
synLSHQ–LSHQ	0.06 ± 0.01	0.90 ± 0.02	synLSHQ	26.59 ± 1.72	0.57 ± 0.06
synLSHQ versus HSLQ	$p < 0.01$	$p < 0.01$		$p < 0.01$	$p < 0.01$

LSHQ, LSHQ images; HSLQ, HSLQ images; synLSHQ, synthetic LSHQ images; nMAE, normalized mean absolute error; SSIM, structural similarity index measurement; PSNR, peak signal-to-noise ratio; EKI, edge keeping index

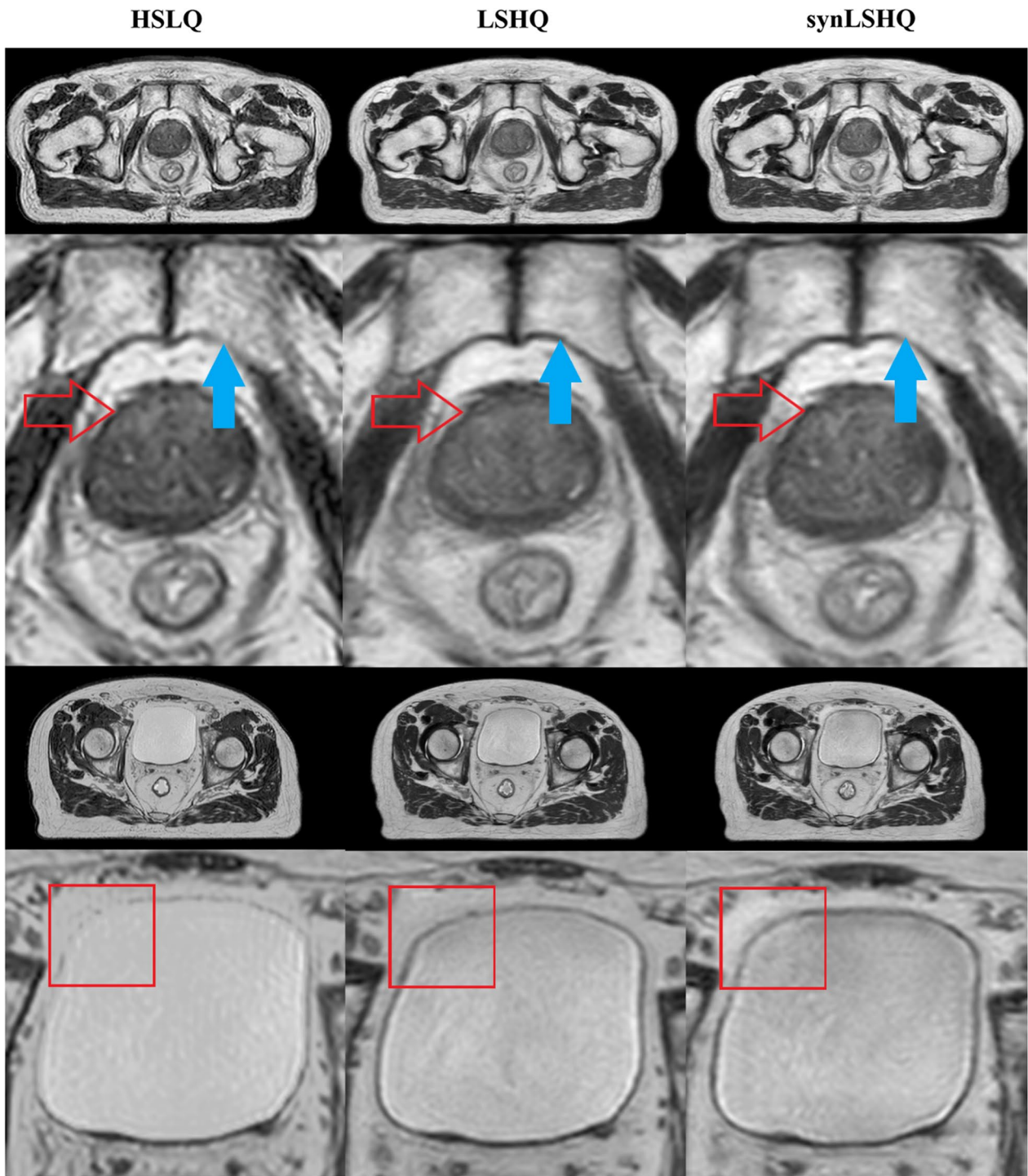


Fig. 4 Examples of HSLQ, LSHQ, and synLSHQ images. First column: HSLQ; Second column: LSHQ; Third column: synLSHQ. Red arrow: boundary of the prostate; Sky blue arrow: boundary of the pubic symphysis; Red box: boundary of bladder

Registration accuracy

The Jacobian determinant and geometric indices (DSC and MDA) were performed to analyze the registration accuracy for each transformation. When deformed to

reference planning CT images, the JDVs for the HSLQ and synLSHQ images were 0.83 ± 0.07 and 0.88 ± 0.04 , respectively. The *p*-value was less than 0.01 and the synLSHQ images exhibited a higher mean JDV by 0.05

compared with the HSLQ images. These results indicate that deformed synLSHQ images experience less expansion and shrinking compared with deformed HSLQ images.

Examples of the CTV, bladder, rectum, left femur head, and right femur head are shown in Fig. 5. The results of contours from the synLSHQ images are significantly close to that of the reference planning CT images. The DSC and MDA results of OARs for each transformation are shown in Fig. 6. On average, the synLSHQ images improved the DSC of the CTV, rectum, left femur head,

and right femur head by 0.01 ($p > 0.05$), 0.03 ($p < 0.05$), 0.01 ($p < 0.05$), and 0.02 ($p < 0.05$), respectively, and reduced the MDA of the CTV, rectum, left femur head, and right femur head by 0.13 mm ($p > 0.05$), 0.24 mm ($p < 0.05$), 0.11 mm ($p < 0.05$), and 0.22 mm ($p < 0.05$), respectively, compared with the HSLQ images. Meanwhile, the equivalent contours error of the bladder ($p > 0.05$ for both DSC and MDA) were obtained from the HSLQ and synLSHQ images. These results demonstrate that the volumetric overlap ratio of the synLSHQ and planning CT images was higher compared with that of

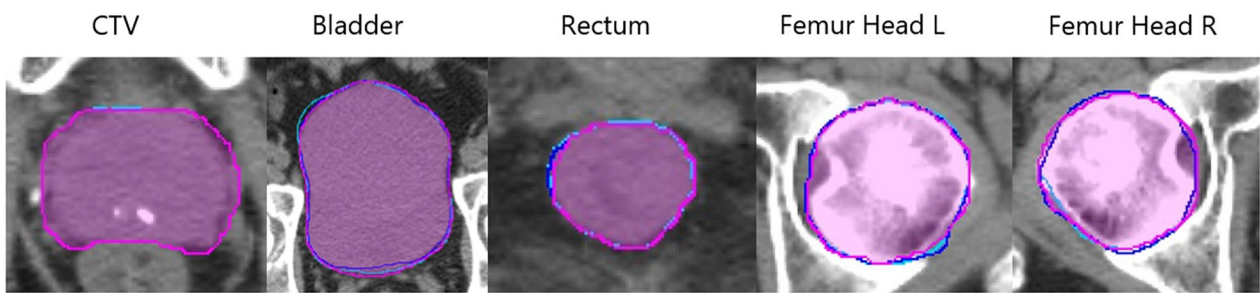


Fig. 5 Examples of contours transferred to reference planning CT images. Purple colorwash: contours on planning CT image; Dark Blue line: contours on T2 HSLQ image; Sky blue line: contours on the T2 synLSHQ image

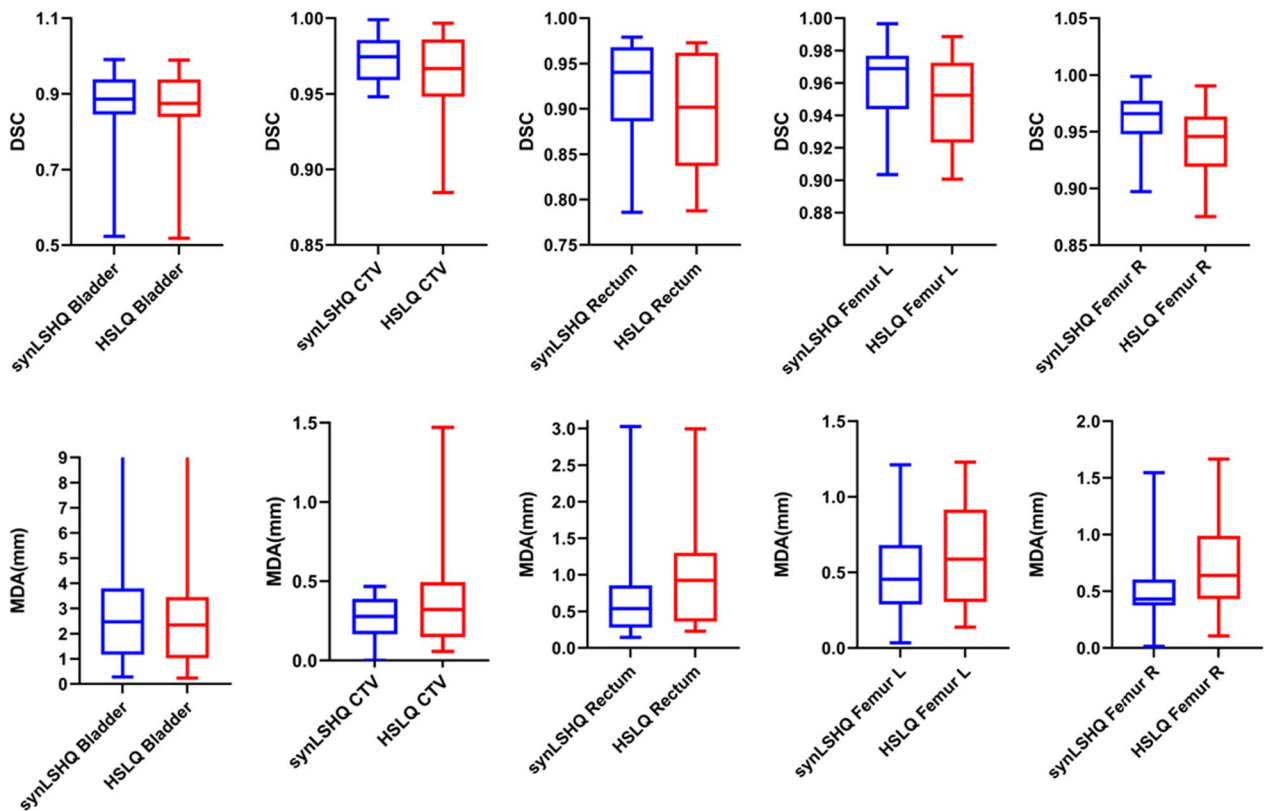


Fig. 6 DSC and MDA box plots for the manual contours on the T2 HSLQ and synLSHQ images with respect to the reference planning CT images

the HSLQ and planning CT images. The Jacobian determinant and the geometric indices demonstrate that the proposed synLSHQ can improve the registration accuracy compared with HSLQ images.

Discussion

MRI guided adaptive radiotherapy is a useful technique; however, its time-consuming nature presents a significant challenge. The long period of adaptive treatment often affects patient comfort—especially patients with diminished bladder capacity. Moreover, long scan times also introduce motion artefact in MR imaging. These limitations impede the application of MRI guided adaptive radiotherapy. To improve patients' comfort and reduce motion artefact, it is important to decrease the duration of each step of adaptive radiotherapy. The proposed synLSHQ has the potential to effectively address this challenge. In one case, our proposed method saved 66% of the total generation time. With process optimization and hardware development, this method has the potential to further improve efficiency to reduce high-quality MRI acquisition time.

There was improvement in nMAE (57%), SSIM (3.4%), PSNR (26.9%), and EKI (3.6%) compared with the HSLQ images. Overall, synLSHQ generated by the proposed method enhances the registration accuracy with a superior mean JDV (6%) and preferable geometric indices.

Several studies have demonstrated the feasibility of deep learning methods for synthesizing high-resolution MR images from low-resolution MR images [8, 12, 25]. Most of the paired data for training and validation was generated using down-sampling post-processing method in previous studies. In our study, we proposed a deep learning-based data augmentation technique to overcome the problem of limited size and diversity of training data in clinic. And then we proposed an effective fine-tune method by using real paired data from the MR-linac to generate high-quality synthetic MRI images.

The proposed method showed potential for MRI guided adaptive treatment of prostate cancer. For the application, the first step is to obtain under-sampled MRI images using the HSLQ sequence. Then the synLSHQ images are generated through the proposed model by inputting HSLQ images. Finally, synLSHQ images are registered to planning CT images to determine whether to perform online adaptive radiotherapy process. As shown in the above application scenarios, the proposed method can significantly reduce scan time while ensuring image quality compared with LSHQ sequence.

Several limitations should be considered in our study. Because of lack of enough real-world data, an augmentation technique was used in training of the proposed model. There is no fully real-world data-based model

compared with the proposed model. Fully real-world data-based model is meaningful for generating high quality MR in short time for precision radiotherapy in future work. The proposed method was tested with data collected in our department. External validation will be required before implementing our proposed model on other MR-linac machines. Meanwhile, our proposed model was trained for prostate cancer. Other models which are trained using data from other types of cancer should be carefully evaluated before clinical use.

Conclusion

In conclusion, we proposed a novel method to improve image quality and registration accuracy for accelerated 3D imaging with a 1.5 T MRI radiotherapy system. It generates high-quality MRI images from HSLQ scanning sequences to significantly shorten the scan time while ensuring the accuracy of radiotherapy.

Abbreviations

MRI	Magnetic resonance imaging
GAN	Generative adversarial network
CycleGAN	Cycle-consistent GAN
LSHQ	Low-speed, high-quality
HSLQ	High-speed, low-quality
synLSHQ	Synthetic LSHQ
TR	Repetition time
TE	Echo time
FOV	Field of view
NAS	Number of signal averaged
nMAE	Normalized mean absolute error
PSNR	Peak signal-to-noise ratio
SSIM	Structural similarity index measurement
EKI	Edge keeping index
CTV	Clinical target volume
OARs	Organs at risk
JDV	Jacobian determinant value
DSC	Dice similarity coefficient
MDA	Mean distance to agreement

Supplementary Information

The online version contains supplementary material available at <https://doi.org/10.1186/s13014-023-02306-4>.

Additional file 1. Appendix.

Acknowledgements

Not applicable

Author contributions

JZ did the data analysis and Writing; XC was another major contributor in writing the manuscript; YL and BY performed the validation of the model; RW performed the data augmentation model; ZY contoured and checked the OARs; SQ and ZH collected and prepared the data; JD reviewed and edited the manuscript; KM created the ideas, formulated research goals and methodology.

Funding

This work was supported by the National Natural Science Foundation of China (11975313, 12005302). The Beijing Nova Program (Z201100006820058). Beijing Natural Science Foundation (7222149).

Availability of data and materials

The raw data supporting the conclusions of this article will be made available by the authors, without undue reservation.

Declarations

Ethics approval and consent to participate

For this study anonymized patient data was used. According to our local ethics committee this does not require ethics approval.

Consent for publication

Not applicable.

Competing interests

The authors declare that they have no competing interests.

Author details

¹National Cancer Center, National Clinical Research Center for Cancer, Cancer Hospital, Chinese Academy of Medical Sciences and Peking Union Medical College, Beijing 100021, China. ²School of Physics and Technology, Wuhan University, Wuhan 430072, China.

Received: 13 January 2023 Accepted: 21 June 2023

Published online: 01 July 2023

References

- Kontaxis C, Woodhead PL, Bol GH, Lagendijk JJW, Raaymakers BW. Proof-of-concept delivery of intensity modulated arc therapy on the Elekta Unity 1.5 T MR-linac. *Phys Med Biol*. 2021;66:041t1.
- Lagendijk JJ, Raaymakers BW, van Vulpen M. The magnetic resonance imaging-linac system. *Semin Radiat Oncol*. 2014;24:3.
- Raaymakers BW, Jürgenliemk-Schulz IM, Bol GH, Glitzner M, Kotte ANTJ, Van Asselen B, et al. First patients treated with a 1.5 T MRI-Linac: clinical proof of concept of a high-precision, high-field MRI guided radiotherapy treatment. *Phys Med Biol*. 2017;62:L41–50.
- Winkel D, Bol GH, Kroon PS, van Asselen B, Hackett SS, Werensteijn-Honingh AM, et al. Adaptive radiotherapy: the Elekta Unity MR-linac concept. *Clin Transl Radiat Oncol*. 2019;18:54–9.
- Bruijnen T, Stemkens B, Lagendijk JJW, van den Berg CAT, Tijssen RHN. Multiresolution radial MRI to reduce IDLE time in pre-beam imaging on an MR-Linac (MR-RIDDLE). *Phys Med Biol*. 2019;64: 055011.
- Zhang Y, Cheng JZ, Xiang L, Yap PT, Shen D. Dual-Domain Cascaded Regression for Synthesizing 7T from 3T MRI. In: *Medical image computing and computer-assisted intervention: MICCAI International Conference on Medical Image Computing and Computer-Assisted Intervention*. 2018. vol. 11070, p. 410–7.
- Lustig M, Donoho D, Pauly JM. Sparse MRI: the application of compressed sensing for rapid MR imaging. *Magn Reson Med*. 2007;58:1182–95.
- Mardani M, Gong E, Cheng JY, Vasanawala SS, Zaharchuk G, Xing L, et al. Deep generative adversarial neural networks for compressive sensing MRI. *IEEE Trans Med Imaging*. 2019;38:167–79.
- Alexander DC, Zikic D, Zhang J, Zhang H, Criminisi A. Image quality transfer via random forest regression: applications in diffusion MRI. In: *Medical image computing and computer-assisted intervention: MICCAI International Conference on Medical Image Computing and Computer-Assisted Intervention*. 2014. vol. 17, p. 225–32.
- Chartsias A, Joyce T, Giuffrida MV, Tsiftaris SA. Multimodal MR synthesis via modality-invariant latent representation. *IEEE Trans Med Imaging*. 2018;37:803–14.
- Wu Y, Ma Y, Capaldi DP, Liu J, Zhao W, Du J, et al. Incorporating prior knowledge via volumetric deep residual network to optimize the reconstruction of sparsely sampled MRI. *Magn Reson Imaging*. 2020;66:93–103.
- Kim KH, Do WJ, Park SH. Improving resolution of MR images with an adversarial network incorporating images with different contrast. *Med Phys*. 2018;45:3120.
- Quan TM, Nguyen-Duc T, Jeong WK. Compressed sensing MRI reconstruction using a generative adversarial network with a cyclic loss. *IEEE Trans Med Imaging*. 2018;37:1488–97.
- Liu F, Feng L, Kijowski R. MANTIS: model-augmented neural network with incoherent k-space sampling for efficient MR parameter mapping. *Magn Reson Med*. 2019;82:174–88.
- Zhu JY, Park T, Isola P, Efros AA. Unpaired image-to-image translation using cycle-consistent adversarial networks. In: *IEEE*. 2017.
- Isola P, Zhu J, Zhou T, Efros AA. Image-to-image translation with conditional adversarial networks. In: *2017 IEEE Conference on Computer Vision and Pattern Recognition (CVPR)*, p. 5967–76.
- Rao RB, Fung G. On the dangers of cross-validation. An experimental evaluation. In: *Proceedings of the SIAM International Conference on Data Mining, SDM 2008, April 24–26, 2008, Atlanta*.
- Wang W, Lu Y. Analysis of the mean absolute error (MAE) and the root mean square error (RMSE) in assessing rounding model. *lop Conf*. 2018;324:012049.
- Xie H, Lei Y, Wang T, Roper J, Dhabaan AH, Bradley JD, et al. Synthesizing high-resolution magnetic resonance imaging using parallel cycle-consistent generative adversarial networks for fast magnetic resonance imaging. *Med Phys*. 2021;49:357.
- Wang Z, Bovik AC, Sheikh HR, Simoncelli EP. Image quality assessment: from error visibility to structural similarity. *IEEE Trans Image Process Publ IEEE Signal Process Soc*. 2004;13:600–12.
- Wang T, Lei Y, Fu Y, Wynne JF, Curran WJ, Liu T, et al. A review on medical imaging synthesis using deep learning and its clinical applications. *J Appl Clin Med Phys*. 2021;22:11–36.
- Bhadauria HS, Dewal ML. Image denoising based on adaptive fusion of curvelet transform and total variation. *Int J Signal Imaging Syst Eng*. 2011;4:220.
- Brock KK, Mutic S, McNutt TR, Hua L, Kessler ML. Use of image registration and fusion algorithms and techniques in radiotherapy: report of the AAPM radiation therapy committee task group No. 132. *Med Phys*. 2017;44:e43.
- McKenzie EM, Santhanam A, Ruan D, O'Connor D, Cao M, Sheng K. Multimodality image registration in the head-and-neck using a deep learning-derived synthetic CT as a bridge. *Med Phys*. 2020;47:1094–104.
- Galbusera F, Bassani T, Casaroli G, Gitto S, Zanchetta E, Tta E, Costa F, et al. Generative models: an upcoming innovation in musculoskeletal radiology? A preliminary test in spine imaging. *Eur Radiol Exp*. 2018;2:1–13.

Publisher's Note

Springer Nature remains neutral with regard to jurisdictional claims in published maps and institutional affiliations.

Ready to submit your research? Choose BMC and benefit from:

- fast, convenient online submission
- thorough peer review by experienced researchers in your field
- rapid publication on acceptance
- support for research data, including large and complex data types
- gold Open Access which fosters wider collaboration and increased citations
- maximum visibility for your research: over 100M website views per year

At BMC, research is always in progress.

Learn more biomedcentral.com/submissions

